

Nonlocal Kinetic Energy Density Functionals for Isolated Systems via Local Density Approximation Kernels

Qiang Xu[†], Jian Lv[†], Yanchao Wang^{*,†}, and Yanming Ma^{*,†,#}

[†] *Innovation Center of Computational Physics Methods and Software & State Key Lab of Superhard Materials, College of Physics, Jilin University, Changchun 130012, China.*

[#] *International Center of Future Science, Jilin University, Changchun 130012, China*

Corresponding Authors:

**E-mail: wyc@calypso.cn*

**E-mail: mym@calypso.cn*

Despite a large number of nonlocal kinetic energy density functionals (KEDFs) available for large-scale calculations, most of those nonlocal KEDFs designed for the extended systems cannot be directly applied to isolated systems. In this manuscript, we proposed a generalized scheme to construct nonlocal KEDFs via the local density approximation kernels and construct a family of KEDFs for simulations of isolated systems within orbital-free density functional theory. The performance of KEDFs has been demonstrated by several clusters encompassing Mg, Si and GaAs. The results show that our constructed KEDFs can achieve high numerical accuracy and stability for random clusters, therefore, making orbital-free density functional theory accessible for practical simulations of isolated systems.

1. Introduction

Ab initio calculation based on density functional theory (DFT)^{1,2} as a prevalent tool for materials simulation has provided important insights into a variety of materials. Particularly, orbital-free (OF) DFT has been recognized as a practical means for large-scale simulations, as exemplified by the calculations of simple metals containing millions of atoms in simulated cell³⁻⁵. However, the accuracy of OF-DFT heavily depends on the approximation of kinetic energy density functional (KEDF) since the kinetic energy is the same order of magnitude as the total energy. Therefore, the main barrier to widespread use of OF-DFT is the lack of reliable KEDFs with high transferability and numerical stability.

In the past few decades, a large number of KEDFs including local/semilocal and nonlocal KEDFs have been available. The local/semilocal KEDFs such as Thomas-Fermi (TF)⁶⁻⁸, von Weizsäcker (vW)⁹, generalized gradient approximation¹⁰⁻¹⁹, and meta-generalized gradient approximation^{20,21} functionals are constructed using the local electron density or its gradient and Laplacian. These functionals can be easily applied to isolated systems²²⁻²⁵. However, local/semilocal functionals cannot reproduce the quantum oscillation of electron density, such as atomic shell structure^{20,26} and Friedel oscillations^{27,28}. In order to capture the quantum oscillation of electron density, several nonlocal KEDFs such as Wang-Teter (WT)²⁹, Smargiassi-Madden (SM)³⁰, Perrot³¹ and Mi-Genova-Pavanello (MGP)³², etc.^{28,33} have been proposed by employment of density-independent kernels with a constant Fermi wave vector (FWV) of $k_F^0 = (3\pi^2\rho_0)^{1/3}$. However, the constant FWV is usually related to the average density (ρ_0) in the unit cell for extended systems and is not well defined in isolated systems²¹.

To avoid using the constant FWV, the density-dependent weight function or kernel are employed in several nonlocal KEDFs including Chacón-Alvarelos-Tarazona (CAT)²⁷, Wang-Govind-Carter (WGC)³⁴ and Huang-Carter (HC)³⁵. However, they suffer from poor transferability or numerical instability problems for isolated systems³⁶. Furthermore, the solution of differential equations is required to make these KEDFs recover the linear response of uniform electron gas, which is inappropriate for modeling

of isolated systems. A nonlocal functional with propagator-like kernel proposed by Wang and Teter successfully reproduced the atomic shell structures²⁹. However, this KEDF required artificial introduction of Gaussian functions with fitting parameters. Later, the advanced nonlocal KEDFs have been proposed and used to simulate the isolated systems³⁷⁻⁴². Particularly, a family of nonlocal KEDFs named LX ($X=WT, MGP0, MGP$) were recently constructed using the numerical local density approximated approach. The LX KEDFs were proved to achieve close to chemical accuracy and high transferability for clusters³⁶. Unfortunately, these KEDFs still suffer from the numerical instability in some cases.

In this manuscript, a generalized scheme has been proposed to construct KEDFs for isolated systems by introduction of the local density-dependent kernels and a variety of nonlocal KEDFs have been constructed within the scheme. We have implemented these KEDFs into ATLAS⁴³ for numerical calculations of isolated systems within OF-DFT. The high accuracy and numerical stability of these KEDFs have been demonstrated by successful applications to several clusters.

The remainder of this manuscript is organized as follows. Section 2 briefly gives the OF-DFT, followed by the detailed scheme for construction of KEDFs and their implementation into ATLAS. The computational details are provided in Section 3. The accuracy and numerical stability of the proposed KEDFs for simulations of isolated systems have been demonstrated in section 4. Finally, we give conclusions in Section 5.

2. Theory and Implementation

2.1 Orbital-free density functional theory

In OF-DFT, the ground-state energy E_{GS} and electron density ρ_{GS} are obtained by minimizing the total energy functional $E[\rho]$ of the N_e -electron system⁴⁴

$$E_{GS}[\rho_{GS}] = \min_{\rho} \left\{ E[\rho] - \mu \left(\int_{\Omega} \rho(\vec{r}) d^3r - N_e \right); \rho \geq 0 \right\}, \quad (1)$$

where ρ is the electron density and μ denoting the Lagrange multiplier is used to enforce the constraint that the total number of electrons. The total energy density functional $E[\rho]$ can be written as

$$E[\rho] = T_s[\rho] + E_H[\rho] + E_{ie}[\rho] + E_{xc}[\rho] + E_{ii}(R), \quad (2)$$

where T_s , E_H , E_{ie} , E_{xc} , E_{ii} and R denote terms of noninteracting kinetic energy, the Hartree energy, the ion-electron interaction energy, the exchange-correlation energy, the ion-ion repulsion energy and the collection of ionic positions, respectively. In contrast to Kohn-Sham (KS) DFT, where the exact noninteracting kinetic energy term is evaluated by single-particle orbitals, OF-DFT relies upon explicit functionals of the electron density for all energy terms.

2.2 The nonlocal KEDFs for isolated systems

Most of nonlocal KEDFs can be written in the generic form

$$T_s[\rho] = T_{TF}[\rho] + T_{vW}[\rho] + T_{NL}^X[\rho], \quad (3)$$

where $T_{TF}[\rho] = \frac{3}{10}(3\pi^2)^{2/3} \langle \rho^{5/3}(\vec{r}) \rangle$ and $T_{vW}[\rho] = \frac{1}{8} \left\langle \frac{|\nabla \rho(\vec{r})|^2}{\rho(\vec{r})} \right\rangle$ are the Thomas-

Fermi⁶⁻⁸ and von Weizsäcker⁹ KEDFs, respectively. The last term in Eq. (3) is the nonlocal part of KEDFs. A simplest form of nonlocal part of KEDFs is expressed as Eq.

(4) and includes a density-independent kernel $w_{\alpha,\beta}^X$.

$$T_{NL}^X[\rho] = \left\langle \rho^\alpha(\vec{r}) \left| w_{\alpha,\beta}^X \left[k_F^0, \vec{r} - \vec{r}' \right] \right| \rho^\beta(\vec{r}') \right\rangle, \quad (4)$$

where α and β are positive parameters that define $X=WT$ ²⁹, MGP and MGP0³² for $\alpha = \beta = 5/6$, $X=SM$ ³⁰ for $\alpha = \beta = 1/2$ and $X=Perrot$ ³¹ for $\alpha = \beta = 1$.

In our scheme, we reformulate the nonlocal term of KEDFs by introduction of the local density approximation kernels (LDAK). Specifically, the constant k_F^0 in density-independent kernel of KEDFs of Eq. (4) is directly substituted by local FWV of $k_F(\vec{r}) = (3\pi^2 \rho(\vec{r}))^{1/3}$. In other words, a density-dependent kernel related to the local electron density instead of average electron density is employed in our scheme.

Within this scheme, the nonlocal terms of KEDFs in Eq. (4) are reformulated as

$$T_{NL}^{LDAK-X}[\rho] = \langle \rho^\alpha(\vec{r}) | w_{\alpha,\beta}^X [k_F(\vec{r}), \vec{r} - \vec{r}'] | \rho^\beta(\vec{r}') \rangle, \quad (5)$$

The corresponding kinetic energy potentials (KEPs) are given by

$$\begin{aligned} V_{T,NL}^{LDAK-X}[\rho] = & \alpha \rho^{\alpha-1}(\vec{r}) \int w_{\alpha,\beta}^X [k_F(\vec{r}), \vec{r} - \vec{r}'] \rho^\beta(\vec{r}') d^3 r' \\ & + \rho^\alpha(\vec{r}) \int \frac{dw_{\alpha,\beta}^X [k_F(\vec{r}), \vec{r} - \vec{r}']}{d\rho(\vec{r})} \rho^\beta(\vec{r}') d^3 r' \\ & + \beta \rho^{\beta-1}(\vec{r}') \int w_{\alpha,\beta}^X [k_F(\vec{r}'), \vec{r} - \vec{r}'] \rho^\alpha(\vec{r}) d^3 r'. \end{aligned} \quad (6)$$

2.3 The implementation of OF-DFT for isolated systems

The previous version of ATLAS code has been used for numerical calculations of periodic systems within OF-DFT⁴³. The long-range electrostatic interactions (ion-ion, ion-electron, and electron-electron interactions) under the periodic boundary conditions are evaluated by introduction of an artificial supercell with large vacuum for isolated systems⁴⁵⁻⁴⁷. However, it usually leads to slow convergence of the total energy with supercell size if there are the strong multipole-multipole interactions between the periodic replicas⁴⁸.

Herein, a capability for simulations of isolated clusters has been implemented in ATLAS code, where the long-range electrostatic interactions are calculated under the Dirichlet boundary condition (DBC). In general, all the electrostatic energy terms can be calculated with a linear scaling under DBC except for the ion-ion interaction term.

The ion-ion interaction energy in Eq. (2) is defined as

$$E_{ii}(\mathbf{R}) = \sum_{I=1}^{N_a} \sum_{J>I}^{N_a} \frac{Z_I Z_J}{R_{IJ}}, \quad (7)$$

where N_a is the number of atoms, $R_{IJ} = |\vec{R}_I - \vec{R}_J|$. $\{\vec{R}_I\}$ and $\{Z_I\}$ denote the ionic positions and charges, respectively. Obviously, a direct calculation of ion-ion interaction shows an intrinsic square scaling with respect to the number of ions. In fact,

the Eq. (2) can also be reformulated as^{49,50}

$$E[\rho] = T_s[\rho] + E_{xc}[\rho] + E_{ele}[\rho, R], \quad (8)$$

where E_{ele} denoting the electrostatic interaction energy contains the ion-ion, ion-electron, and electron-electron interactions. The electrostatics can be expressed by^{49,51,52}:

$$E_{ele}[\rho, R] = \sup_{V_{ele}} \left\{ -\frac{1}{8\pi} \int |\nabla V_{ele}(\vec{r})|^2 d^3r + \int (\rho(\vec{r}) + b(\vec{r})) V_{ele}(\vec{r}) d^3r \right\} - E_{self}(R) + E_c(R), \quad (9)$$

where V_{ele} is referred as the electrostatic potential, b is the total pseudo-charge density of the nuclei, E_{self} is the self-energy of nuclei, E_c is used to correct the error of ion-ion repulsive energy due to overlap of pseudo-charge density. The electrostatic potential V_{ele} in Eq. (9) is calculated by solving the Poisson equation:

$$\nabla^2 V_{ele}[n](\vec{r}) = -4\pi n(\vec{r}). \quad (10)$$

The total density of n is defined as the sum of pseudo-charge density and electron density

$$n(\vec{r}) = \rho(\vec{r}) + b(\vec{r}). \quad (11)$$

The detailed calculations of b , E_{self} and E_c can be found in Ref. 49.

In this work, the electron density distribution and the corresponding electrostatic potentials are represented on real-space discrete Cartesian grid points. Just as shown in Fig. 1(a), the radius R_{\max} of a spherical region is used to truncate the tail of electron density, whose value should be zero beyond the spherical region. The electrostatic potentials are directly represented on discretized grid points in cubic cell. Note that the unit cell length edge is defined as $L = 2R_{\max}$. There are two types of grid points in our implementation as illustrated in Fig. 1(b). The electrostatic potentials on boundary points are calculated by the multipoles expansion method⁵³, whereas the electrostatic potentials on the internal points can be solved by conjugate gradient iteration with

multigrid in real space⁵⁴. The number of boundary layers is determined by the order of finite difference. For efficient linear-scaling calculations of $T_{NL}^{LDAK-X}[\rho]$ and the corresponding potentials $V_{T,NL}^{LDAK-X}[\rho]$, the integrals of $P(\vec{r}) = \int w[k_F(\vec{r}), |\vec{r} - \vec{r}'|] f(\vec{r}') d^3 r'$ and $Q(\vec{r}) = \int w[k_F(\vec{r}), |\vec{r} - \vec{r}'|] f(\vec{r}') d^3 r'$ in Eqs. (5) and (6) are calculated by cubic Hermite spline interpolation technique and fast Fourier transform (FFT)³⁵. It is important to note that the computational cost of Eqs. (5) and (6) becomes intrinsic quasilinear scaling $O[mN \log N]$. Note that m and N are the number of uniform interpolation nodes of FWs and FFT grids, respectively. The details of these techniques are provided in Ref. 35. The ground-state electron density is obtained by minimizing the total energy using the truncated Newton method⁵⁵ and more details can be found in Ref. 43.

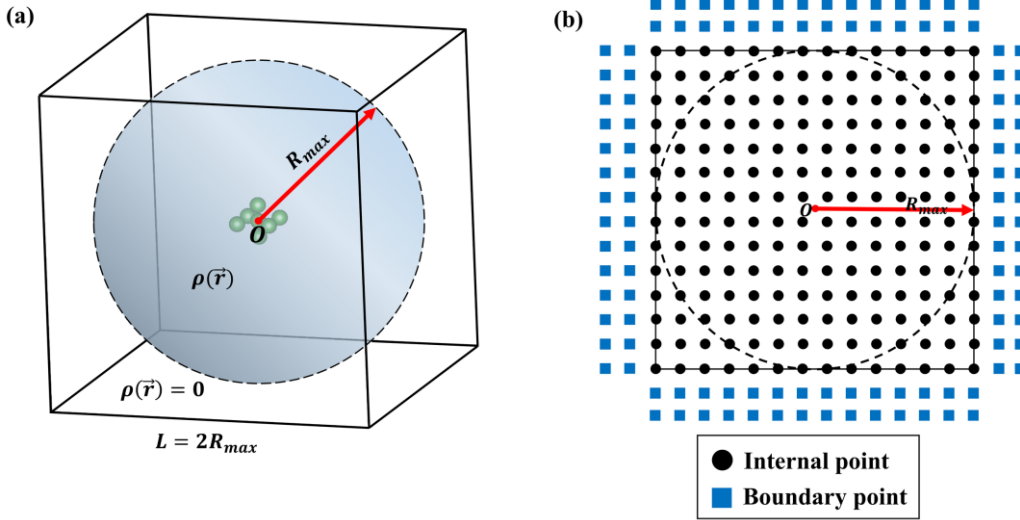


Fig. 1. The schematic illustrations of ATLAS implementation. (a) The electron density distribution in cubic cell. (b) Two-dimensional diagram showing the different types of discretized grid points.

3. Computational details

The OF-DFT calculations with LDAK- X and LX functionals were carried out by ATLAS. A grid spacing of 0.2 Å and eighth finite-difference order gave well convergence of total energies less than 1 meV/atom. The parameter $A=0.2$ of MGP³⁶ was kept fixed for both LDAK-MGP and LMGP. The number of interpolation nodes of

40 and 100 in LDAK- X for clusters of Mg and Si/GaAs gave total energies convergence within 5 meV/atom. Calculations involving the CAT KEDF, in which kinetic energy cutoff of 1600eV, $\rho^* = 0.20 \text{ \AA}^{-3}$ and $\gamma = 1.4$, are performed with PROFESS 3.0³. The KS-DFT calculations were performed by in-house developed ARES software package⁵⁶ and double checked using CASTEP⁵⁷. A grid spacing of 0.2 \AA and 16th finite-difference order in ARES and kinetic energy cutoff of 940 eV for CASTEP were sufficient for a well-converged total energy (1 meV/atom). The bulk-derived local pseudopotentials⁵⁸ and local density approximate exchange and correlation as parametrized by Perdew and Zunger⁵⁹ were employed to estimate the ion-electron and the exchange-correlation interactions for all the considered systems. The structures of Mg₈, Mg₅₀, Ga₄As₄, Ga₂₅As₂₅ and Si₅₀ were randomly generated by CALYPSO^{60,61}. The settings of $R_{\text{max}} = 9.5 \text{ \AA}$ for Mg₈ and Ga₄As₄ and $R_{\text{max}} = 13.0 \text{ \AA}$ for Mg₅₀, Ga₂₅As₂₅, Si₅₀ and Si₆₀ yielded good convergence of total energy.

4. Results and Discussion

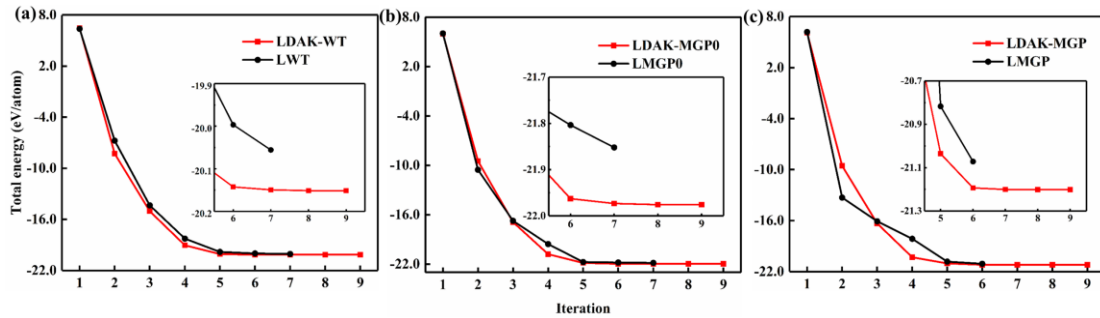


Fig. 2. The comparison of total energy convergence for Mg₈ between LDAK- X and LX, where X denotes (a) WT, (b) MGP0 and (c) MGP, respectively.

To assess the performance of our LDAK- X scheme, we firstly construct a family of KEDFs and perform the energy minimization of Mg₈ using OF-DFT with these KEDFs. For comparison, we also include the results of LX (X =WT, MGP0 and MGP).

Just as shown in Fig. 2, our LDAK- X KEDFs show a significant improvement of numerical stability in comparison with LX KEDFs. For example, it only requires seven iterations to give total energy convergence less than 1 meV/atom for a random structure of Mg_8 using LDAK-MGP in Fig. 2(c), whereas it fails to converge using LMGP³⁶.

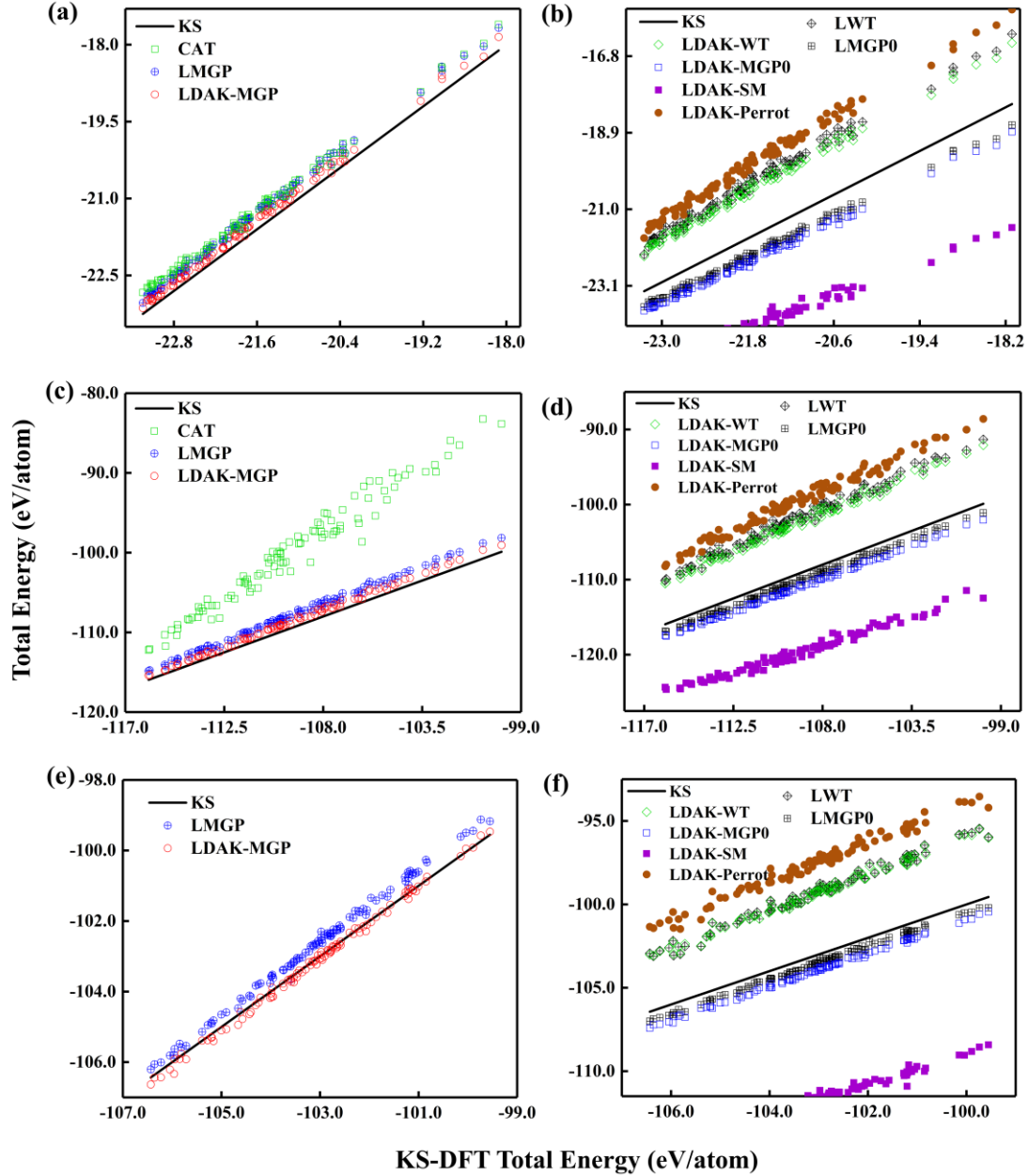


Fig. 3. The total energies of 100 random clusters calculated by OF-DFT with a variety of KEDFs in comparison with the reference KS-DFT results for (a)-(b) Mg_8 , (c)-(d) Ga_4As_4 and (e)-(f) Si_{50} , respectively.

The different converged behaviors of LDAK- X and LX KEDFs originate from their

different mathematic frameworks. Just as presented in Eqs. (6) and (12), the formulas of KEPs for LDK- X and LX schemes are remarkably different. In the LX scheme, the KEPs are calculated by spline interpolation³⁶

$$\begin{aligned} V_{T,NL}^{LX}[\rho](\vec{r}) &= \frac{5}{3} \rho^{-1/6}(\vec{r}) \int w^X [k_F(\vec{r}), |\vec{r} - \vec{r}'|] \rho^{5/6}(\vec{r}') d^3 r' \\ &= \frac{5}{3} \rho^{-1/6}(\vec{r}) \sum_{i=1}^m c_i [\rho(\vec{r}), \vec{r}] \int w^X [k_i, |\vec{r} - \vec{r}'|] \rho^{5/6}(\vec{r}') d^3 r', \end{aligned} \quad (12)$$

where $\{c_i\}$ denotes the spline interpolation coefficients and $\{k_i\}$ is the set of interpolation nodes. Note that those coefficients depend on the local density $\rho(\vec{r})$. In general, KEDF can be obtained by direct integration of KEP. However, it suffers from high computational costs due to involving the extremely complicated integrations. A simple approximation, which regards $\{c_i\}$ as density-independent parameters, was employed in the LX scheme³⁶ to obtain the KEDF by line integral from the KEP in Eq. (12). However, this approximation is so strong that the derivative relation between KEDF and KEP cannot be strictly satisfied. Hence LX KEDFs suffer from numerical instabilities during energy minimization for some cases. In contrast, LDK- X KEDFs are constructed by direct introduction of local density dependent kernels and the corresponding KEP is obtained by derivative of KEDF. Therefore, the derivative relation between KEDF and KEP is strict, making LDK- X functionals numerically stable during energy minimization.

To evaluate the accuracy of LDK- X , total energies of 100 random structures of Mg₈, Ga₄As₄ and Si₅₀ clusters were evaluated by OF-DFT with various KEDFs including LDK-WT, LDK-MGP0, LDK-MGP, LDK-SM, LDK-Perrot, LWT, LMGP0, LMGP and CAT functionals. The calculated OF-DFT energies in comparison with that

of KS-DFT are shown in Fig. 3. OF-DFT calculations within LDAK- X and LX KEDFs generally produce similar trends of total energies as KS-DFT for all considered systems. Especially, LDAK-MGP and LMGP show a significant improvement in computational accuracy compared to other functionals. The performance of CAT functional is quite modest for Mg₈ clusters [Fig. 3(a)], while the total energies obtained by CAT functional and KS-DFT show an apparent discrepancy for Ga₄As₄ clusters [Fig. 3(c)]. Particularly, the energy minimization of random structures of Si₅₀ clusters fails to converge using CAT functional.

Table 1. The mean-unsigned-error (MUE) of the total energies (eV/atom) and the mean-unsigned-relative-error (MURE) of electron density in percentage points (in parentheses) with respect to the KS-DFT results for 100 random structures of Mg₈, Ga₄As₄ and Si₅₀. The underline highlights the results close to KS-DFT.

KEDF	MUE of energy (MURE of density)		
	Mg ₈	Ga ₄ As ₄	Si ₅₀
LWT	1.444 (7.8)	7.281 (8.1)	3.744 (4.4)
LMGP0	0.501 (8.8)	1.054 (10.3)	0.512 (8.3)
LMGP	0.313 (7.7)	1.528 (10.0)	0.457 (8.6)
LDAK-SM	2.406 (31.2)	10.444 (30.6)	8.547 (29.8)
LDAK-Perrot	1.969 (9.9)	9.649 (12.7)	5.535 (8.9)
LDAK-WT	1.295 (8.3)	6.719 (9.9)	3.701 (7.6)
LDAK-MGP0	0.650 (7.1)	1.818 (6.5)	0.931 (<u>3.5</u>)
LDAK-MGP	<u>0.164</u> (<u>6.9</u>)	<u>0.766</u> (<u>6.3</u>)	<u>0.086</u> (<u>3.5</u>)
CAT	0.370 (9.7)	9.522 (17.5)	-

In order to further quantify the accuracy of KEDFs, we defined unsigned-error of total energy $\Delta E_i = \frac{1}{N_a} |E_i^{OF} - E_i^{KS}|$ and unsigned-relative-error of electron density

$\Delta \rho_i = \frac{1}{N_e} \int |\rho_i^{OF}(\vec{r}) - \rho_i^{KS}(\vec{r})| d^3r$ for i -th cluster. The mean-unsigned-error of total

energies $\overline{\Delta E} = \frac{1}{100} \sum_{i=1}^{100} \Delta E_i$ and the mean-unsigned-relative-error of electron density

$$\overline{\Delta\rho} = \frac{1}{100} \sum_{i=1}^{100} \Delta\rho_i \quad \text{for 100 random structures of Mg}_8, \text{Ga}_4\text{As}_4 \text{ and Si}_{50} \text{ are listed in Table}$$

1. It is apparent that LDAK-MGP outperforms other KEDFs and yields the smallest $\overline{\Delta E}$ and $\overline{\Delta\rho}$ in all considered cases. Furthermore, it should be stressed that energy minimization using LDAK-MGP is able to obtain high convergence rates approaching 100% for all the random structures, which is superior to that of LX³⁶.

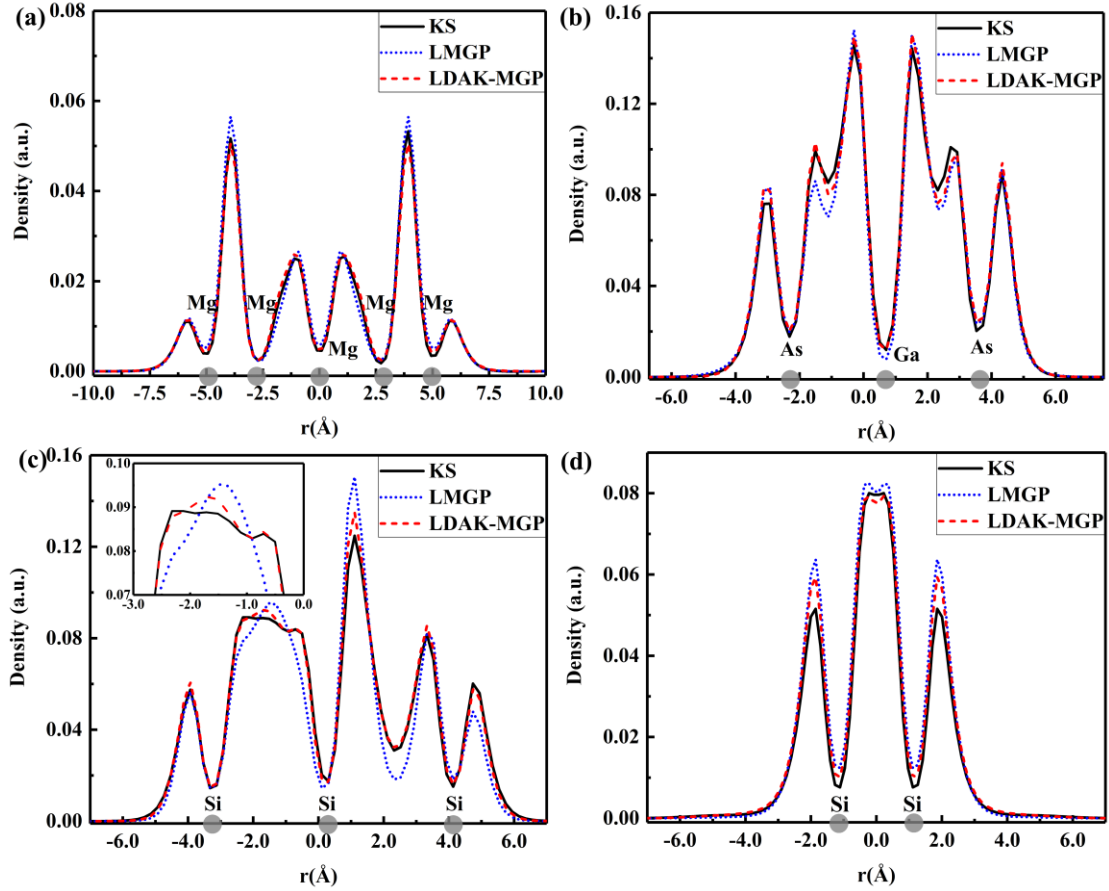


Fig. 4. The electron densities calculated by LMGP (blue dot), LDAK-MGP (red short dash) and KS-DFT (black solid line) for (a) Mg₅₀ (b) Ga₂₅As₂₅ (c) Si₅₀ and (d) Si₆₀ along the specific bond orientation.

In addition, we also evaluated electron densities of Mg₅₀, Ga₂₅As₂₅, Si₅₀ and Si₆₀ using LDAK-MGP in comparison with those estimated by LMGP, as well as KS-DFT. The detailed structural information and the corresponding directions for each structure are presented in the Supplemental Material⁶². As shown in Fig. 4, the electron density

distributions predicted by LDAK-MGP shares the similar general shapes with KS-DFT in the all regions, while LMGP gives quite different distributions for the bonding regions and near-core regions. It is important to note that LDAK-MGP successfully reproduces the tiny density oscillation obtained by KS-DFT in the bonding region for Si_{50} , as evidenced by insert of Fig. 4(c). These results reveal that LDAK-MGP gives more accurate distributions of electron density for isolated systems than those obtained by LMGP.

5. Conclusion

In summary, a LDAK- X scheme derived from the local density approximation is proposed to construct a family of nonlocal KEDFs for isolated systems. These KEDFs have been implemented into the ATLAS package and showed superior performance to other KEDFs both numerical accuracy and stability for several clusters encompassing Mg, Si and GaAs. The LDAK-MGP with high accuracy and numerical stability makes OF-DFT as the most promising approach for simulations of isolated systems.

Acknowledgements Y. W. and Y. M. acknowledge funding support from the National Key Research and Development Program of China under Grant No. 2016YFB0201201, and 2017YFB0701503; the National Natural Science Foundation of China under Grants No. 11404128, 11822404, 11534003 and 11774127; supported by Program for JLU Science and Technology Innovative Research Team (JLUSTIRT); and the Science Challenge Project, No. TZ2016001. Part of the calculation was performed in the high-performance computing center of Jilin University. We thank Mi Wenhui for helpful discussions.

Reference

- ¹ P. Hohenberg and W. Kohn, Phys. Rev. **136**, B864 (1964).
- ² W. Kohn and L.J. Sham, Phys. Rev. **140**, A1133 (1965).

- ³ M. Chen, J. Xia, C. Huang, J.M. Dieterich, L. Hung, I. Shin, and E.A. Carter, *Comput. Phys. Commun.* **190**, 228 (2015).
- ⁴ M. Chen, X.W. Jiang, H. Zhuang, L.W. Wang, and E.A. Carter, *J. Chem. Theory Comput.* **12**, 2950 (2016).
- ⁵ X. Shao, Q. Xu, S. Wang, J. Lv, Y. Wang, and Y. Ma, *Comput. Phys. Commun.* **233**, 78 (2018).
- ⁶ L.H. Thomas, *Math. Proc. Cambridge Philos. Soc.* **23**, 542 (1927).
- ⁷ E. Fermi, *Rend. Accad. Naz. Lincei* **6**, 602 (1927).
- ⁸ E. Fermi, *Z. Phys.* **48**, 73 (1928).
- ⁹ C.F. von Weizsäcker, *Z. Phys.* **96**, 431 (1935).
- ¹⁰ H. Ou-Yang and M. Levy, *Int. J. Quantum Chem.* **40**, 379 (1991).
- ¹¹ A.J. Thakkar, *Phys. Rev. A* **46**, 6920 (1992).
- ¹² J.P. Perdew, *Phys. Lett. A* **165**, 79 (1992).
- ¹³ L. Vitos, B. Johansson, J. Kollár, and H.L. Skriver, *Phys. Rev. A* **61**, 052511 (2000).
- ¹⁴ M. Ernzerhof, *J. Mol. Struct. Theochem.* **501–502**, 59 (2000).
- ¹⁵ L.A. Constantin and A. Ruzsinszky, *Phys. Rev. B* **79**, 115117 (2009).
- ¹⁶ L.A. Constantin, E. Fabiano, S. Laricchia, and F. Della Sala, *Phys. Rev. Lett.* **106**, 186406 (2011).
- ¹⁷ S. Laricchia, E. Fabiano, L.A. Constantin, and F. Della Sala, *J. Chem. Theory Comput.* **7**, 2439 (2011).
- ¹⁸ A. Lembarki and H. Chermette, *Phys. Rev. A* **50**, 5328 (1994).
- ¹⁹ K. Luo, V. V. Karasiev, and S.B. Trickey, *Phys. Rev. B* **98**, 041111(R) (2018).
- ²⁰ D. García-Aldea and J.E. Alvarellos, *J. Chem. Phys.* **127**, 144109 (2007).
- ²¹ L.A. Constantin, E. Fabiano, and F. Della Sala, *J. Phys. Chem. Lett.* **9**, 4385 (2018).
- ²² A. Aguado, J.M. López, J.A. Alonso, and M.J. Stott, *J. Chem. Phys.* **111**, 6026 (1999).
- ²³ A. Aguado, *Phys. Rev. B* **63**, 115404 (2001).
- ²⁴ A. Aguado, J.M. López, J.A. Alonso, and M.J. Stott, *J. Phys. Chem. B* **105**, 2386 (2001).

- ²⁵ G.K.-L. Chan, A.J. Cohen, and N.C. Handy, *J. Chem. Phys.* **114**, 631 (2001).
- ²⁶ E. Engel and R.M. Dreizler, *J. Phys. B* **22**, 1901 (1989).
- ²⁷ E. Chacón, J.E. Alvarellos, and P. Tarazona, *Phys. Rev. B* **32**, 7868 (1985).
- ²⁸ Y.A. Wang, N. Govind, and E.A. Carter, *Phys. Rev. B* **58**, 13465 (1998).
- ²⁹ L.W. Wang and M.P. Teter, *Phys. Rev. B* **45**, 13196 (1992).
- ³⁰ E. Smargiassi and P.A. Madden, *Phys. Rev. B* **49**, 5220 (1994).
- ³¹ F. Perrot, *J. Phys. Condens. Matter* **6**, 431 (1994).
- ³² W. Mi, A. Genova, and M. Pavanello, *J. Chem. Phys.* **148**, 184107 (2018).
- ³³ A. Aguado, D.J. González, L.E. González, J.M. López, S. Núñez, and M.J. Stott, in *Recent Progress in Orbital-Free Density Functional Theory* (World Scientific, Singapore, 2013) Chap. 4, pp. 55–145.
- ³⁴ Y.A. Wang, N. Govind, and E.A. Carter, *Phys. Rev. B* **60**, 16350 (1999).
- ³⁵ C. Huang and E.A. Carter, *Phys. Rev. B* **81**, 045206 (2010).
- ³⁶ W. Mi and M. Pavanello, *Phys. Rev. B* **100**, 041105(R) (2019).
- ³⁷ N. Choly and E. Kaxiras, *Solid State Commun.* **121**, 281 (2002).
- ³⁸ D. García-Aldea and J.E. Alvarellos, *Phys. Rev. A* **76**, 052504 (2007).
- ³⁹ G.S. Ho, C. Huang, and E.A. Carter, *Curr. Opin. Solid State Mater. Sci.* **11**, 57 (2007).
- ⁴⁰ G.S. Ho, V.L. Lignères, and E.A. Carter, *Phys. Rev. B* **78**, 045105 (2008).
- ⁴¹ J. Xia, C. Huang, I. Shin, and E.A. Carter, *J. Chem. Phys.* **136**, 084102 (2012).
- ⁴² J. Xia and E.A. Carter, *Phys. Rev. B* **86**, 235109 (2012).
- ⁴³ W. Mi, X. Shao, C. Su, Y. Zhou, S. Zhang, Q. Li, H. Wang, L. Zhang, M. Miao, Y. Wang, and Y. Ma, *Comput. Phys. Commun.* **200**, 87 (2016).
- ⁴⁴ G.S. Ho, V.L. Lignères, and E.A. Carter, *Comput. Phys. Commun.* **179**, 839 (2008).
- ⁴⁵ J.R. Chelikowsky, N. Troullier, and Y. Saad, *Phys. Rev. Lett.* **72**, 1240 (1994).
- ⁴⁶ J.R. Chelikowsky, N. Troullier, K. Wu, and Y. Saad, *Phys. Rev. B* **50**, 11355 (1994).
- ⁴⁷ C.A. Rozzi, D. Varsano, A. Marini, E.K.U. Gross, and A. Rubio, *Phys. Rev. B* **73**, 205119 (2006).
- ⁴⁸ A. Castro, A. Rubio, and M.J. Stott, *Can. J. Phys.* **81**, 1151 (2003).

- ⁴⁹ S. Ghosh and P. Suryanarayana, *Comput. Phys. Commun.* **212**, 189 (2017).
- ⁵⁰ S. Das, M. Iyer, and V. Gavini, *Phys. Rev. B* **92**, 014104 (2015).
- ⁵¹ J.E. Pask and P.A. Sterne, *Phys. Rev. B* **71**, 113101 (2005).
- ⁵² P. Suryanarayana and D. Phanish, *J. Comput. Phys.* **275**, 524 (2014).
- ⁵³ W.R. Burdick, Y. Saad, L. Kronik, I. Vasiliev, M. Jain, and J.R. Chelikowsky, *Comput. Phys. Commun.* **156**, 22 (2003).
- ⁵⁴ W. Hackbusch, *Multi-grid Methods and Applications*, Springer Series in Computational Mathematics, Vol. 4 (Springer-Verlag, Berlin, Heidelberg, 1985).
- ⁵⁵ S.G. Nash, *J. Comput. Appl. Math.* **124**, 45 (2000).
- ⁵⁶ Q. Xu, S. Wang, L. Xue, X. Shao, P. Gao, J. Lv, Y. Wang, and Y. Ma, *J. Phys. Condens. Matter* **31**, 455901 (2019).
- ⁵⁷ M.D. Segall, *J. Phys. Condens. Matter* **14**, 2717 (2002).
- ⁵⁸ C. Huang and E.A. Carter, *Phys. Chem. Chem. Phys.* **10**, 7109 (2008).
- ⁵⁹ J.P. Perdew and A. Zunger, *Phys. Rev. B* **23**, 5048 (1981).
- ⁶⁰ Y. Wang, J. Lv, L. Zhu, and Y. Ma, *Phys. Rev. B* **82**, 094116 (2010).
- ⁶¹ Y. Wang, J. Lv, L. Zhu, and Y. Ma, *Comput. Phys. Commun.* **183**, 2063 (2012).
- ⁶² See the Supplemental Material at <http://link.aps.org/supplemental/10.1103/PhysRevB.101.045110> for the POSCAR files of Mg₅₀, Ga₂₅As₂₅, Si₅₀ and Si₆₀ clusters in Fig. 4 and total energies of 20 random structures of Al₅₀ clusters are evaluated by ATLAS under Dirichlet boundary condition and periodic boundary condition.